Materials and Design 88 (2015) 1234–1243

Contents lists available at ScienceDirect

Materials and Design

journal homepage: www.elsevier.com/locate/jmad

Toughening mechanisms and mechanical properties of graphene nanosheet-reinforced alumina

Iftikhar Ahmad [a,*], Mohammad Islam [a], Hany Sayed Abdo [a], Tayyab Subhani [b], Khalil Abdelrazek Khalil [c], Abdulhakim A. Almajid [c], Bahareh Yazdani [d], Yanqiu Zhu [d]

[a] Deanship of Scientific Research, Advanced Manufacturing Institute, King Saud University, P.O. Box 800, Riyadh 11421, Saudi Arabia
[b] Composite Research Center, Department of Materials Science and Engineering, Institute of Space Technology, Islamabad, Pakistan
[c] Department of Mechanical Engineering, King Saud University, P.O. Box 800, Riyadh 11421, Saudi Arabia
[d] College of Engineering, Mathematics and Physical Sciences, University of Exeter, Exeter EX4 4QF, UK

ARTICLE INFO

Article history:
Received 3 June 2015
Received in revised form 20 September 2015
Accepted 21 September 2015
Available online 25 September 2015

Keywords:
Ceramic matrix composites
Nanocomposites
HFIHS
Induction sintering
Graphene nanosheets
GNS
Fracture toughness
Interface

ABSTRACT

High-frequency induction heat sintering (HFIHS) technology was employed for fabrication of highly dense (>99.5%) graphene-reinforced alumina nanocomposites. The mixed powders were consolidated at temperatures up to 1500 °C with 0.25 to 3.0 wt.% exfoliated graphene nanosheets (GNS). Compared with monolithic alumina, there was grain size refinement by 46% with an associated increase in the fracture toughness (by 72%) and hardness values (7%). Electron microscopy revealed that exfoliated GNS retained their inherent planar structure against any possible chemical and/or thermal adverse effect caused by rapid sintering. The intrinsic 2-dimensional sheet morphology and flexibility of the GNS promoted formation of large Al_2O_3/GNS interfacial area, thus leading to a dominant reinforcing mechanism via grain anchoring. The presence of GNS at the grain boundary areas not only inhibited grain growth through pinning effect, it also modified friction traits at nanoscale level by inducing slip–stick phenomenon that increased the Al_2O_3/GNS interfacial strength by means of improved efficiency of graphene pull-out and crack-bridging that subsequently imparted toughness and altered the failure behavior of the composites. A possible correlation between GNS incorporation into Al_2O_3 matrix and the resulting mechanical properties is established through high-resolution TEM studies that indicated graphene/alumina interface formation without any presence of severe intermediate phases.

© 2015 Published by Elsevier Ltd.

1. Introduction

Numerous strategies have been explored to alleviate the brittleness issue of monolithic alumina (Al_2O_3) in order to broaden the scope of this promising structural ceramic from conventional industrial uses to advanced engineering applications including aerospace components, space vehicles, missiles, automobiles and other military products [1–4]. To meet this challenge, intensive attention had been focused on the development of nanostructures-reinforced Al_2O_3 matrix composites technology over the past decade. Earlier attempts to produce Al_2O_3-based composites containing ceramic or metallic whiskers, fibers or particulates could not satisfy the requirement of their direct use as structural components [5,6]. Incorporation of carbon nanotubes (CNT) into Al_2O_3 has, to a certain extent, led to improvements in toughness, strength and other mechanical properties in recent years [7–11]. However, the exceptional strength and elasticity associated with one-dimensional CNT still could not be fully exploited for Al_2O_3 due to technical challenges including CNT agglomeration, inadequate densification processes and poor Al_2O_3/CNT interfacial strength [12–14]. In the wake of breakthroughs in graphene exfoliation technology, it is pertinent that new strategies are devised for addition of the two-dimensional graphene as a novel reinforcement in to different ceramic matrices [15].

Graphene has sp^2 bonded carbon atoms arranged in a planar configuration, and is the stiffest and strongest material known so far. The remarkable mechanical strength, elasticity and unique functional characteristics predicted for graphene suggest that, after being reinforced properly by graphene, the Al_2O_3 ceramic can be converted to a tougher, stronger, stiffer and thermally as well as electrically conductive material [16–18]. As compared to CNT, there are several advantages associated with graphene addition namely larger specific surface area, superior mechanical strength/flexibility, less tendency of entanglement and far more simple to disperse in a ceramic matrix. Besides, graphene synthesis in high yields is easier, more economical and poses less health hazards than those of CNT [19–21], making it an ideal candidate to replace CNT in nanocomposites. A review of the published literature indicates that most of the work thus far focused on graphene reinforcement in the Si_3N_4 ceramic and polymer matrices with few studies on Al_2O_3 matrix [15,22]. For 1.5 and 3.0 vol.% graphene additions into Si_3N_4, an increase in the fracture toughness (K_{IC}) values by 235 and 45% was

* Corresponding author.
E-mail address: ifahmad@ksu.edu.sa (I. Ahmad).

http://dx.doi.org/10.1016/j.matdes.2015.09.125
0264-1275/© 2015 Published by Elsevier Ltd.

reported [22,23]. In case of Al_2O_3 based composites, moderately higher fracture toughness values, by 27, 28, 33 and 53%, were reported for composites containing 0.3 [15] and 0.8 vol.% graphene [24] and 0.22 [25] and 2.0 wt.% graphene [26]. A recent approach involving use of both graphene and carbon nanotubes was employed by Yazdani et al. to produce high performance Al_2O_3 nanocomposites using hot pressing technique with reported increase in the fracture toughness and flexural strength values by 63 and a 15% [27].

One of the potential drawbacks associated with conventional pressureless sintering and hot-pressing (HP) techniques for ceramic composite fabrication are chemical/thermal deterioration of the graphene crystalline quality and grain growth of the matrix materials due to prolonged heating cycle [16,27]. To eliminate these issues, novel sintering techniques involving relatively lower sintering temperatures and/or reduced dwell times at elevated temperatures, have been explored [28], rapid spark-plasma sintering (SPS) process one of them for fabrication of Al_2O_3/graphene nanocomposite [22–26]. Another relatively new rapid sintering technology is high-frequency induction heat sintering (HFIHS) process that enables rapid heating to desirable consolidation temperatures and has been successfully utilized for consolidation and sintering of several metallic, monolithic ceramics and composite powders to near theoretical densities. After spark plasma sintering, HFIHS is a new addition in high-temperature ceramic powder compaction, involving consolidation at desirable temperatures in a very short time span after heating at extremely high rate under vacuum and uniaxial pressure. Although the ceramic powder consolidation is carried out in a graphite die like in case of hot-pressing, the heating is done using high-frequency power source to drive large alternative current through a Cu induction coil surrounding the graphite mold [28]. In this way, the HFHIS provides a right amount of heat to the loose composite powders quickly for them to attain maximum possible densification under pressure with minimum damage to the primary structures of the nanocomposite constituents. Unlike mass diffusion and substantial material transportation across grain boundaries as in case of prolonged conduction heat sintering cycles, the HFHIS process relies on Joule heating principle causing creep and localized densification with nominal diffusion/material transportation mechanism [29,30]. Thus far, the exploration of this promising processing route for Al_2O_3/graphene nanocomposites is, however, scarce [31].

In this paper, we report fabrication of Al_2O_3/graphene ceramic matrix nanocomposites containing 0.25 to 3.0 wt.% graphene through HFIHS process, their characterization/testing for investigation of microstructural features and interfacial studies, microhardness and fracture toughness testing, failure analysis and possible structure/property correlation to induce toughening mechanism that may be responsible for properties enhancement in the resulting nanocomposites. The study encompasses thermal exfoliation of graphite flakes to obtain graphene followed by its characterization, mixing of Al_2O_3 and graphene powders and subsequent consolidation via HFIHS process. The Al_2O_3/graphene nanocomposites with different graphene content were examined to assess graphene dispersion into Al_2O_3 matrix and its role towards densification and grain refinement besides improvement in microhardness and fracture toughness without any degradation of the composite constituents.

2. Materials and methodology

2.1. Sample preparation

Using Hummer's method [32], the as-received surface enhanced graphite flakes (Grade-3775, Asbury Graphite Mills Inc., NJ, USA) were first chemically modified to graphite oxide (GO) followed by thermal exfoliation upon heating to 1600 °C at 1000 °C/min and 4.5×10^{-2} Torr pressure in an induction-heat furnace [33]. The graphene nanosheets (GNS) so obtained were then mixed with Al_2O_3 nanopowder (Sigma Aldrich, UK) with an average particle size of <30 nm via an aqueous colloidal technique. For this purpose, designed amounts of GNS were separately added to 100 ml distilled water in the presence of sodium dodecyl sulfate (SDS) as surfactant. The aqueous GNS/SDS slurry was then agitated for 30 min using a sonic probe (Vibracell VCX-750, Sonics, Materials Incorporation, USA) at 750 W power and 20 kHz frequency. The resulting mixture was kept for 2 weeks to ensure thorough adsorption of the SDS onto the GNS surfaces. Another aqueous suspension of the Al_2O_3 nanoparticles was prepared separately from ultrasonic vibration treatment for 30 min. Both GNS/SDS and Al_2O_3 aqueous slurries were mixed with final dispersion/homogeneization treatment in the form of ultrasonic agitation for 60 min by keeping pH value at 10 and then dried at 120 °C. Following this procedure, a batch of 4 g loose composite mixture for each composition was prepared. The dried nanocomposite powders were then consolidated in a graphite die at different conditions of temperatures (1400 and 1500 °C) and uniaxial pressures (30, 50 and 60 MPa) in the HFIHS apparatus (HF Active Sinter System, ELTEK, South Korea). Once adequate vacuum level of 45 mTorr was attained, the desirable load was applied and the temperature was raised at 150 °C/min to certain temperature. The temperature was monitored using an optical pyrometer (Thermalert TX, Raytek GmbH, Germany). In this way, 3 disks of $\phi 10 \times 3$ mm were fabricated for each nanocomposite formulations based on GNS content and pure monolithic Al_2O_3 reference samples were also made under the same processing conditions for comparison purposes.

2.2. Density measurement and structural characterization

Measurement of the apparent densities for all the sintered nanocomposite samples was conducted using the Archimedes method. For relative density calculation, the theoretical densities of Al_2O_3 and GNS were considered to be 3.97 and 2.10 g/cm^3, respectively [14,27]. The X-ray diffraction patterns were obtained by means of an X-ray diffraction system (D-8 Discover, Bruker, Germany) and using CuKα monochromatic radiation. The microstructural examination and grain size measurements, for the polished or thermally etched (1400 °C for 15 min in an inert atmosphere) samples as well as fractured surfaces, were performed by operating a field-emission scanning electron microscope (JSM-7600F, JEOL, Japan), whereas high-resolution electron microscopy of the GNS and the Al_2O_3/GNS interfacial area was carried out using field-emission transmission electron microscope (2100F, JEOL, Japan). For this purpose, the GNS were first dispersed in acetone and then transferred onto holey-carbon Cu grid. On the other hand, for Al_2O_3/GNS interfacial studies, a fine polished nanocomposite sample was further thinned by ion-milling on an ion − slicer (EM 09100, JEOL, Japan).

2.3. Measurement of mechanical properties

The microhardness of all the polished samples was recorded for 9.8 N applied load and 15 s dwell time using a microhardness tester (Buehler-micromet 5114, Akashi corporation, Japan) and the Vickers hardness number (H) values were further converted to GPa [34]. Nanoindentation tests were performed on all the sintered samples using a NanoTest machine (Micro Materials, UK) at 200 mN force and 30 s hold time to allow significant plastic deformation. The nanoindentation technology provides a reliable method to measure the E value of ceramic materials by sensing the penetration depth of indenter at submicron scale. In order to calculate the E value, the maximum load ($Fmax$), the maximum displacement ($hmax$), the elastics contact stiffness ($C = \frac{dF}{dh}$) and the reduced modulus ($E = \frac{\sqrt{\pi}}{2C\sqrt{Ap}}$) values were directly measured from machine recorded load–displacement curve, in unloading condition, according to the method proposed by Oliver and Pharr [35]. Furthermore, to avoid the issues of crack formation during indentation small load (200 mN) were chosen and a fine Berkovich tip indenter

was selected to confine the indentation area within submicron dimensions. Finally the E value for all samples was calculated employing Equation-1 [36]

$$E = \frac{\left[1 - Vs^2\right]}{\left[\frac{1}{E_r} - \frac{\left\{1 - Vi^2\right\}}{E_i}\right]} \quad (1)$$

where V_s and V_i are Possion's ratio for the test specimen and the Berkovich indenter with respective values of 0.23 for monolithic Al_2O_3 and composites and 0.07 for diamond indenter and E_i is the elastic modulus of the diamond indenter (1140 GPa).

The K_{IC} value for all samples was measured using direct crack measurement (DCM) technique. DCM is an attractive technique due to the simplicity and expediency of experiments thus allows estimating the local and bulk fracture properties of the brittle materials like ceramics despite questions on its reliability and accuracy and this issue will be discussed in section 3.5. A Vickers diamond pyramid tip was adopted to produce well-defined radial crack traces on polished ceramic surfaces (in perpendicular direction to the pressure applied during sintering) and the crack lengths for each crack emerging from every corner of an indent during Vickers hardness test were measured using SEM and averaged. For each nanocomposite formulation and monolithic Al_2O_3, at least 10 indents were made. Finally, the elastic modulus (E), microhardness (H), the applied load (P) and the radial crack length (c) were obtained from combined analytical methods and K_{IC} value was computed according to the empirical relationship (Equation-2) proposed by Chantikul et al. [37],

$$K_{IC} = 0.016 \left(\frac{E}{H}\right)^{\frac{1}{2}} \left(\frac{P}{C^{\frac{3}{2}}}\right) \quad (2)$$

3. Results and discussion

3.1. Synthesis and distribution of graphene

The quality and characteristics of the thermally exfoliated GNS was assessed through extensive electron microscopy studies and the findings are presented in Fig. 1. The SEM results (Fig. 1a,b) clearly represent two-dimensional geometrical feature of the GNS with an average lateral dimension of ~2 μm. The thickness of the nanosheet as estimated from the edge of a single GNS (Fig. 1b) is on the order of 3–8 nm. The slight bending of the sheet at the edges and the presence of planar step are also evident in the high magnification image, indicative of the fact that during complex thermal reduction, the GO underwent stern chemical and physical processes prior to splitting into slender arrays of GNS. During transmission electron microscope (TEM) studies, the thickness of the GNS sheet was discerned from the image contrast with light contrast phase representing a single graphene layer (white arrow) and the relatively darker contrast arising from GNS made up of few layers as well as crumpled or wrinkled edges (black arrow). The edge of one such GNS was also viewed at high-resolution (Fig. 1d) and from the cross-section, the thickness of the nanosheet was estimated to be ~7 nm. The rapid thermal exfoliation promotes activities including (i) eradication of the intercalates like H_2O molecules and oxides groups and (ii) rigorous folding/unfolding along with reshuffling of individual graphene layers, under rapid thermal shocks [38]. Despite these chemical and physical actions, microscopic details corroborate that the GNS showed great resistance to degradation and stayed thermally stable against high temperature exfoliation process, maintaining its structural integrity.

In contrast with one-dimensional CNT structures with their tendency towards entanglement [15], the two-dimensional morphology of the GNS makes its dispersibility into the Al_2O_3 matrix relatively less problematic. In case of addition of nanostructures to a ceramic powder, an environment-friendly water based colloidal chemistry route can eliminate the agglomeration issue, if any [39]. For dispersion in aqueous medium, probe-sonication method provided highly energetic sonic

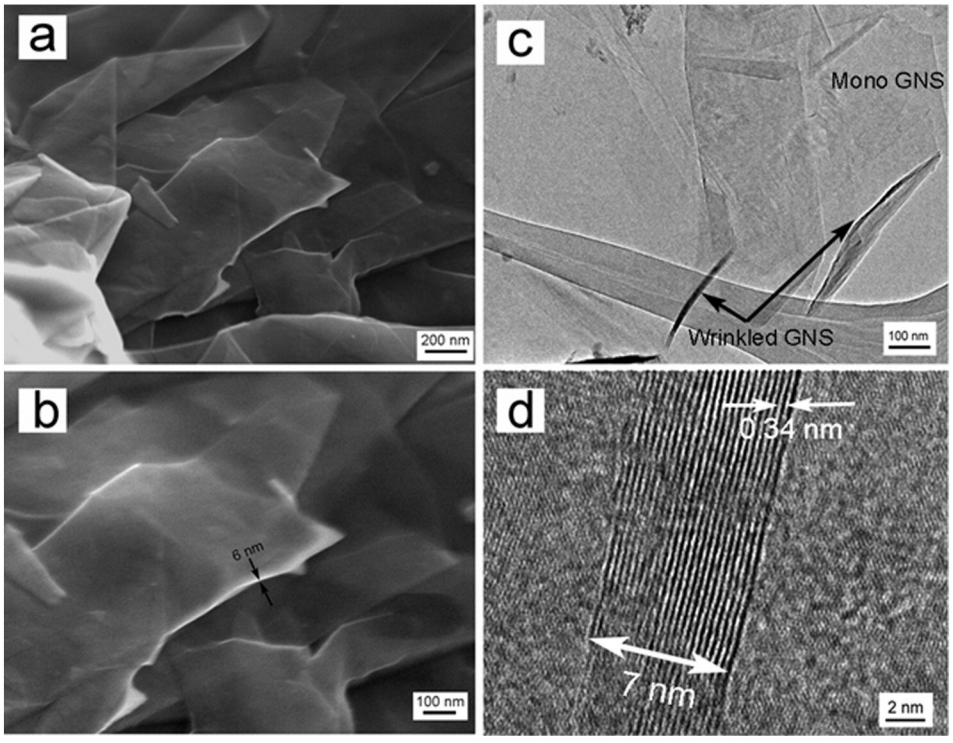

Fig. 1. (a, b) SEM microstructures of thermally exfoliated GNS at low and high magnification representing GNS stacks and its edges; (c, d) TEM micrographs of few wrinkled and folded GNS and high-resolution view of the GNS cross-section with lattice fringe spacing of 0.34 nm.

waves to help disentangle the GNS agglomerates, whereas the SDS surfactant adsorbed on the GNS surfaces ensured homogeneous GNS distribution in the ceramic powder through generation of a positively-charged electrostatic repulsive force for GNS to counteract the van der Waals attraction. The success of this route in obtaining well-dispersed GNS was manifested by TEM and SEM examination of the Al_2O_3/GNS powder mixture and consolidated samples, as shown in Fig. 2. The TEM micrograph represents finely dispersed individual GNS (black arrow) with homogeneous distribution of Al_2O_3 nanoparticles (white arrow) over their surface. The ultrathin nanosheets exhibit smooth surface and, to some extent, folded texture with high area density of the Al_2O_3 nanoparticles. After HFIHS process, the surface of the consolidated nanocomposite samples indicate uniform dispersion of the GNS within the ceramic matrix located at the grain boundaries (Fig. 2b). While relatively large patches of the nanosheets were observed to sandwich between adjacent grains or even bend along the grain boundary area (Fig. 2c) revealing its flexible nature. In some areas, thicker nanosheets seemed to undergo folding giving rise to porosity in the adjacent area (Fig. 2d). Nevertheless, the high values of relative density indicated good densification characteristics during HFIHS process cycle.

3.2. Densification technique and grain size analysis

The density and grain size values for all the samples, consolidated upon heating at 150 °C/min for 3 min dwell time as a HFIHS protocol, are presented in Fig. 3. While monolithic Al_2O_3 samples produced under various sintering HFIHS conditions exhibited near theoretical density without much difficulty, sintering of Al_2O_3/GNS nanocomposites was not that straight-forward. For higher GNS loadings of 1.5 and 3.0 wt.%, the densification was adversely affected at relatively low processing conditions of 1400 °C and 30 MPa. To attain acceptable level of densification, the temperature and applied pressure were raised to 1500 °C and 60 MPa, respectively (Fig. 3a). Fig. 3b depicts the grain size and shape in terms of its length to width ratio for all the samples by demonstrating the influence of GNS content on the Al_2O_3 grains size. There is about 20 and 46% reduction in the average grain size values upon incorporation of 0.25 and 0.5 wt.% GNS, respectively. The GNS addition also seems to promote wrapping of a number of Al_2O_3 nanoparticles by GNS that subsequently prohibit uniform grain coalescence and growth. The average values of grain aspect ratio were derived from measurement of the two sides of several elongated grains thereby obtaining the length-to-width ratio.

While there was no evidence of GNS accumulation, the SEM examination of the fractured nanocomposite surface revealed homogenous GNS dispersion inside ceramic matrix besides GNS bending (black arrows) and wrapping (black circles) around the Al_2O_3 grains (Fig. 2b). In other words, the flexibility of GNS allowed them to bend along and fold around the growing Al_2O_3 grains at elevated temperature and in the presence of high pressure eventually trapping them between adjacent grains. Repeated folding of the GNS increased the space between the matrix grains, thereby preventing them from sealing off the voids or porosity and leading to weakly-coalesced matrix grains. Therefore, nanocomposites sintered at 1400 °C under 30 MPa showed incomplete densification, and became slightly better after the applied pressure was increased to 50 MPa. The research findings imply that external pressure is an important sintering parameter that accelerates the densification process during HFIHS by offering extra driving force for mass transportation and by eliminating the gaps/voids between matrix grains forcing particles to preferential positions with resultant consolidated densities close to the theoretical values.

3.3. Microstructure development and fractography

The effect of GNS addition into Al_2O_3 matrix on grain size of the resulting HFIHS consolidated microstructure was investigated, as manifested by SEM images in Fig. 4. In case of monolithic Al_2O_3, HFIHS process yields a relatively finer microstructure with average size of 1.5 μm (Fig. 4a) than that obtained from hot-pressing [27]. As shown earlier (Fig. 2c), the GNS have a tendency to locate themselves at grain boundaries. While it is deleterious to the densification process on one hand, it

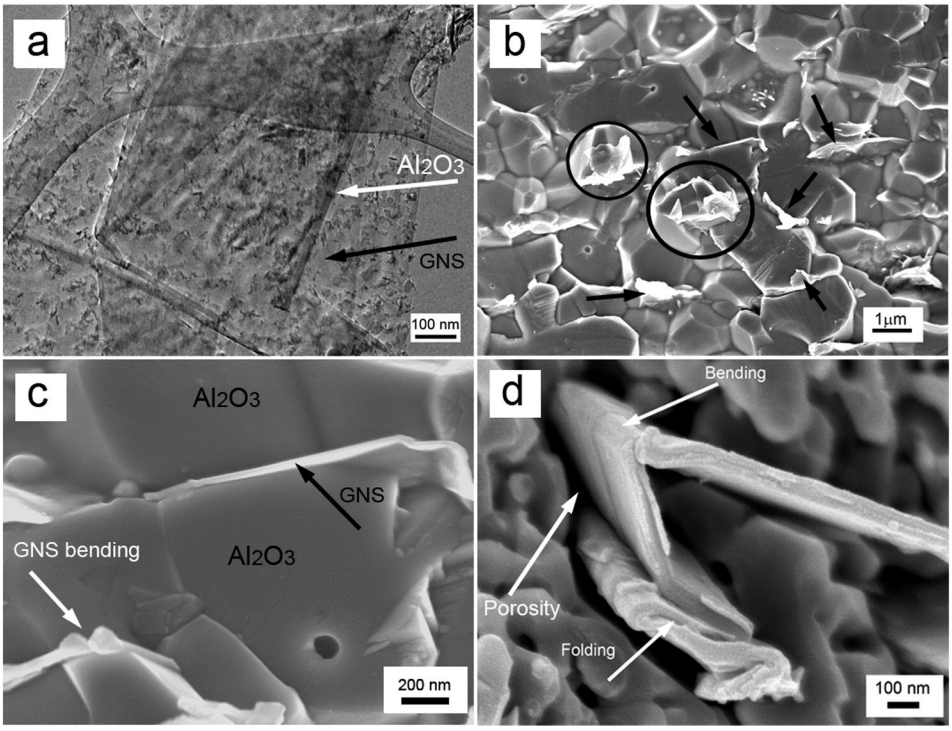

Fig. 2. (a) TEM microstructure of Al_2O_3/GNS powder mixture depicting distribution of Al_2O_3 nanoparticles over GNS and (b-d) Scanning electron microscope images of fractured surfaces of the nanocomposite samples showing (b) homogenous GNS dispersion in the consolidated ceramic matrix, (c) instances of GNS sandwiched between two adjacent grains (black arrow) and (d) High-magnification SEM view illustrating GNS folding and bending and the resulting porosity in its vicinity.

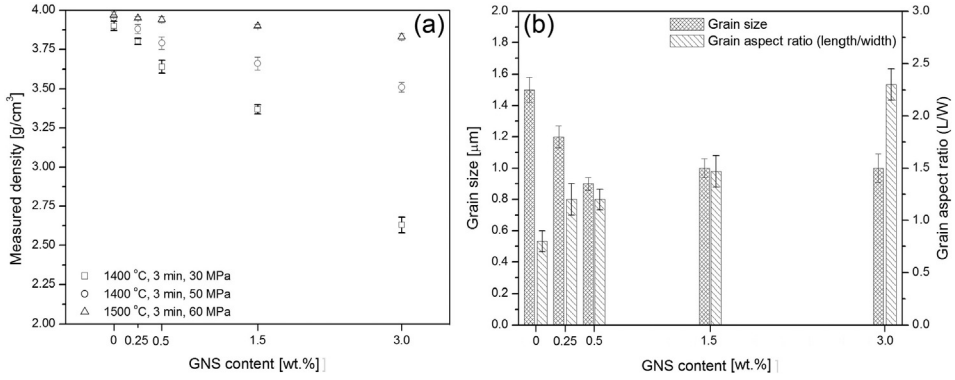

Fig. 3. Graphical representation of the effect of GNS loading level in the nanocomposite on (a) densification behavior of Al_2O_3/GNS nanocomposites for different HFIHS conditions and (b) average size and aspect ratio (L/W) of the matrix grains upon sintering at 1500 °C and 60 MPa for 3 min.

is nevertheless beneficial in obtaining fine-grained microstructures, as evident from the fact that GNS addition by 0.5 wt.% led to grain refinement by 46% (Fig. 3b). The surface microstructure of the Al_2O_3/0.5GNS sample affirms that GNS inhibited grain growth of the Al_2O_3 matrix by wrapping around them, preferably positioning them at grain junctions to produce fine-grained microstructure (Fig. 4b). This finding is also corroborated by another recent report [26,27]. GNS content of 1.5 and 3 wt.% resulted in marginal further grain size refinement (Fig. 4c, d), albeit with evolution of blunt, round and elongated grain morphology instead of prismatic, acicular or needle-like grains strongly embedded into each other as observed in case of monolithic Al_2O_3. It is possible that interconnected GNS would have covered several matrix particles and subsequent high external pressure during sintering integrated them to form elongated morphology via creep. Further statistical analyses (Fig. 3b) of the grain length-to-width ratio (L/W) confirmed GNS contribution in altering the grain morphology, as 3 wt.% GNS in Al_2O_3 produced elongated grains with L/W value of 2.1. In other words, more elongated grains formed in the microstructure of Al_2O_3/3.0GNS sample, as indicated by black arrows in Fig. 4d.

The fractured surfaces of the monolithic as well as nanocomposite Al_2O_3 samples were examined to determine the characteristic fracture mode, as presented by SEM results in Fig. 5. As compared to the intergranular fracture mode seen in case of monolithic Al_2O_3, a notable transformation in the failure mechanism to transgranular fracture was noticed to occur upon up to 0.5 wt.% GNS addition (Fig. 5c). This change suggests that evenly dispersed GNSs firmly bond with Al_2O_3 matrix grains offering support at grain boundaries for efficient stress transfer from one grain to the other. This phenomenon altered the failure propagation route to accrue through matrix grains (transgranular fracture). This is in contrast with weak grain boundary areas in the unreinforced Al_2O_3 where fracture proceeds along the grains causing intergranular failure, as shown in Fig. 5(a). Al_2O_3/GNS nanocomposites containing GNS content of 1.5 or 3 wt.% contained folded and interconnected GNS at matrix grain boundaries (black circled in Fig. 4c and in the inset of Fig. 5d). It appears that these folded GNS behaved like weak/brittle bulk graphite. In the presence of applied load, the folded graphitic planes can readily slip along their basal planes without any dislocation movement. The cracks can, therefore, propagate with relative ease

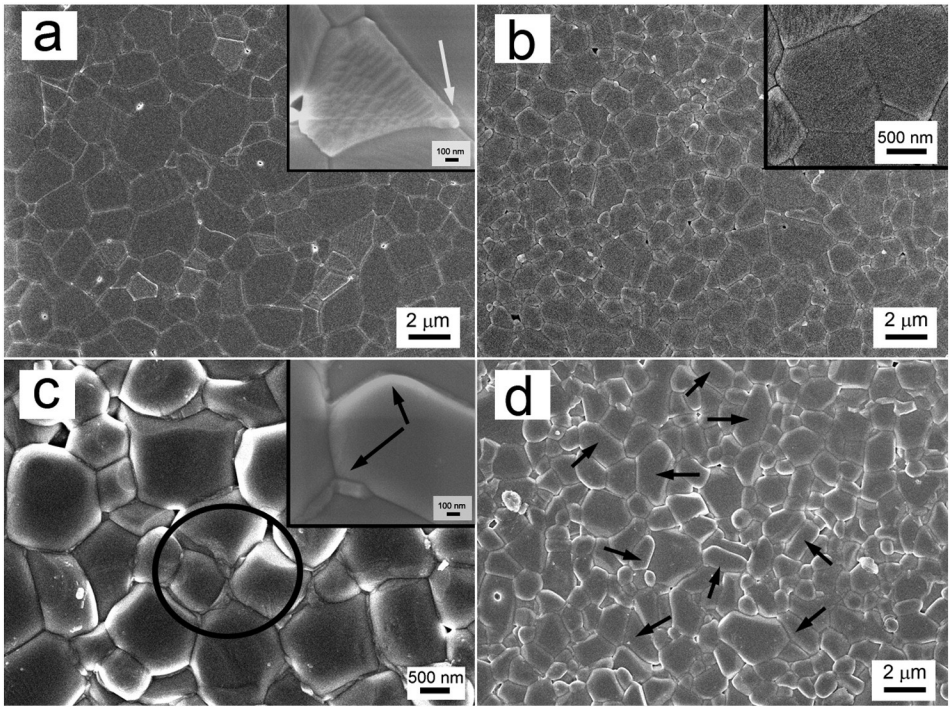

Fig. 4. SEM microstructures of the HFIHS samples after fine Polish and thermal etching, with inset showing high magnification view: (a) monolithic Al_2O_3 showing irregular-shaped grains, (b) Al_2O_3/0.5GNS sample surface presenting fine grain structure, (c, d) Al_2O_3/1.5GNS indicating GNS folding within matrix grains (black circle) with inset showing round/blunt grain morphology and (d) elongated gain morphology (black arrows).

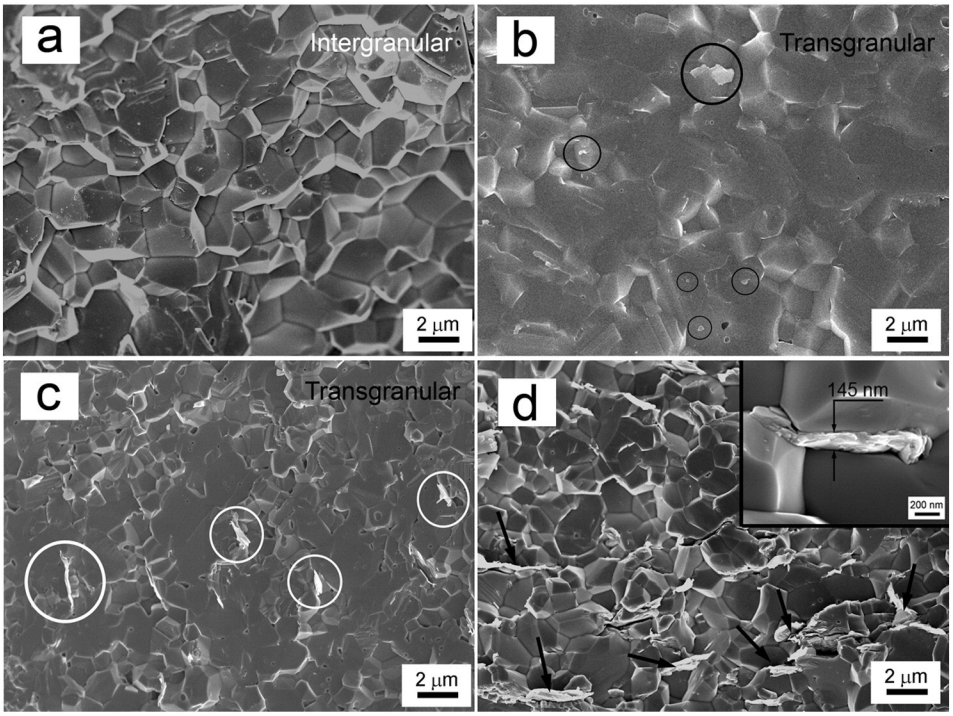

Fig. 5. Fractography of the different ceramic samples indicating peculiar fracture modes: (a) intergranular fracture exhibited by monolithic Al_2O_3, (b) Transgranular fracture in the nanocomposite containing 0.25 wt.% GNS with short pull-out segments of the GNS (black circle), (c) Transgranular fracture mode evident in Al_2O_3/0.5GNS showing larger GNS pull-out segments (white circles), and (d) Al_2O_3/1.5GNS fracture surface indicating several folded GNS and the associated porosity that gave rise to intergranular failure. The inset shows a thicker GNS glut at the boundary of three grains.

through these GNS existing along the grain boundaries, thus causing intergranular fracture mode to be dominant (Fig. 5d) [39,40].

3.4. Influence of GNS on hardness and elastic modulus

As shown in Fig. 6a, the Vickers microhardness values maximized for up to 0.5 wt.% GNS addition followed by a drop for Al_2O_3/GNS nanocomposites containing 1.5 and 3.0 wt.% GNS presumably due to GNS bending, accumulation and rise in porosity level. On the other hand, a progressive decrease in the elastic modulus was noticed with continuous increase in the extent of GNS incorporation. The hardness of the ceramic materials is derived from the microstructure development in terms of size and morphology of the grains. Monolithic ceramics like Al_2O_3 always offer high hardness due to elongated prismatic, acicular or needle-like grain shapes. The incorporation of GNS as a second phase reinforcing medium indeed refined the grain size through grain pinning phenomenon, yet it barely influenced the grain shapes during HFIHS process (see Figs. 3b and 4b). It is a well-known fact that both grain boundary area and reinforcing constituents hinder the onset of plasticity by impeding dislocation movement across the entire nanocomposite microstructure [34]. As compared to monolithic Al_2O_3 samples made under identical conditions, a modest improvement by 4 and 7%, respectively, in the microhardness values was noticed for Al_2O_3/0.25GNS and Al_2O_3/0.5GNS nanocomposite samples.

Interestingly, about 6% and 15% reduction in hardness was noted in Al_2O_3/1.5GNS and Al_2O_3/3.0GNS samples, respectively. This drop in hardness with increased GNS addition may be attributed to the apparent changes in grain shape, intrinsic lubrication characteristics of graphene and residual porosity. It is obvious that round grain morphology appeared in these nanocomposites, Fig. 4d, which could facilitate deformation/sliding of the grains over each other, as rounded grains tend to move easily than faceted ones [41]. Adding on, the presence of residual porosity in the microstructure of nanocomposites may be another contributing factor in depriving the hardness values because the ceramics are sensitive to residual porosity according to a well-known empirical square root relationship ($\sigma_F \propto l^{-0.5}$) which describes the

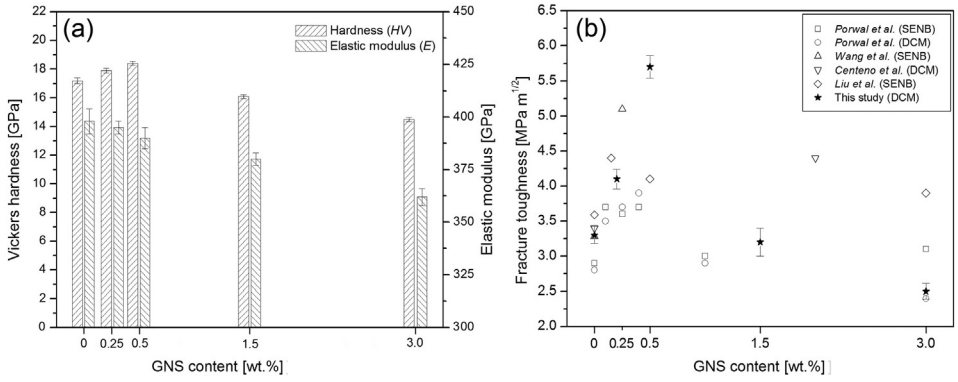

Fig. 6. Effect of GNS incorporation into Al_2O_3 matrix on the mechanical properties of ceramic matrix composites: (a) Fracture toughness and (b) hardness and elastic modulus of the monolithic Al_2O_3 as the function of GNS additions.

fracture strength (σ_F) dependency on the pore size (c) [34]. This corroborates that the residual porosity would have facilitated the crack to initiate at far less load and led nanocomposites, containing higher GNS content, to lower hardness [34]. Furthermore, a gradual drop in the elastic modulus of the nanocomposite samples with greater GNS content (1.5 and 3.0 wt.%) was also observed as represented in Fig. 6a. In this context, Fan et al. suggested that the grain size barley influenced the elastic modulus however, porosity formation around the GNS (Fig. 2) and low modulus of the large GNS along both in-plane and out-of-plan directions are likely to be the foremost reasons behind lower elastic modulus values in these samples [37,44].

3.5. Toughness and reinforcement mechanism

Using DCM technique, K_{IC} values for monolithic Al_2O_3 and Al_2O_3/GNS nanocomposites were determined and compared with other published values, as shown by bar chart in Fig. 6b. While monolithic, unreinforced Al_2O_3 sample yielded a K_{IC} value of 3.3 MPa·m$^{1/2}$, incorporation of 0.25 and 0.50 wt.% GNS resulted in respective K_{IC} values of 4.1 and 5.7 MPa·m$^{1/2}$, an increase by 25 and 72%, respectively. Some reports maintain that the DCM method only provides localized K_{IC} information for test specimen under complex stress field, instead of an absolute K_{IC} value such as that obtained via the standard single-edged notched beam (SENB) method [34]. In this context, several groups strived to curtail this ambiguity by comparing the K_{IC} values obtained from both methods. In case of CNT-reinforced Al_2O_3, Sarkar et al. supported the former technique, whilst Ahmad et al. favored the latter [11,14]. The debate has recently been revived by Porwal et al. [26] who reported negligible discrepancy in the K_{IC} values obtained from both method for Al_2O_3 matrix composites containing low (< 2 vol.%) graphene content, although GNS content greater than this limiting value still led to uncertainties. Beside this, the DCM method offers expediency in the K_{IC} estimation and was, thereby, opted in this work for gauging the betterment against monolithic samples. A gradual increase in the K_{IC} values was seen up to in 0.25 and 0.5 wt.% GNS loading whereas further additions resulted in low K_{IC} values, as shown in Fig. 6b. The fact that several protruded GNS were noticed on the fractured nanocomposite surface (black arrows in Fig. 2b) beside the perfectly embedded GNS within the matrix garins (black arrow in Fig. 2c) implies that the toughening philosphies derived from the fiber-reinforced ceramic composites can also be applicable here, although the GNS pull-out mechanim in the nanocomposites may in essence be more complicated [25,26]. Fig. 2b shows that the GNS are securely wrapped/rolled around the Al_2O_3 grains (black circles), and this uniquely massive interaction allows them to connect with several grains and firmly fasten them together in an intricate manner, leading to the anchoring mechanism. Similar interactions were also identified during our TEM study of the nanocomposites (Fig. 7a). This promising and complex grain anchoring is expected to provide higher interfacial resistance against GNS pull-out from the matrix, thus more energy will be required than that in case of classical pull-out, crack-bridging and crack-deflection toughening mechanisms in nanocomposites [27]. The phenomena of crack deflection and crack bridging by embedded GNS as experienced in the course of crack propagation is highlighted in Fig. 7b.

Further examinations of the fractured nanocomposite surfaces revealed more exciting roles of GNS, via direct and indirect contribution towards toughness enhancement of the nanocomposite. The Al_2O_3/0.25GNS sample exhibited several sheet-like features in the structure, as pointed out by black circles in Fig. 5b. Fig. 8a presents high magnification view of small pull-out segments along with ruptured edges with an estimated thickness of ~7–13 nm which corroborates the efficiency of colloidal chemistry route in suppressing the chances of GNS agglomeration in the nanocomposites. The short pull-out segments also confirmed the resistance for GNS to leave the matrix, implying potentially concurrent actions of GNS anchoring at grain boundaries and strong Al_2O_3/GNS interfacial adhesion, which will be discussed later.

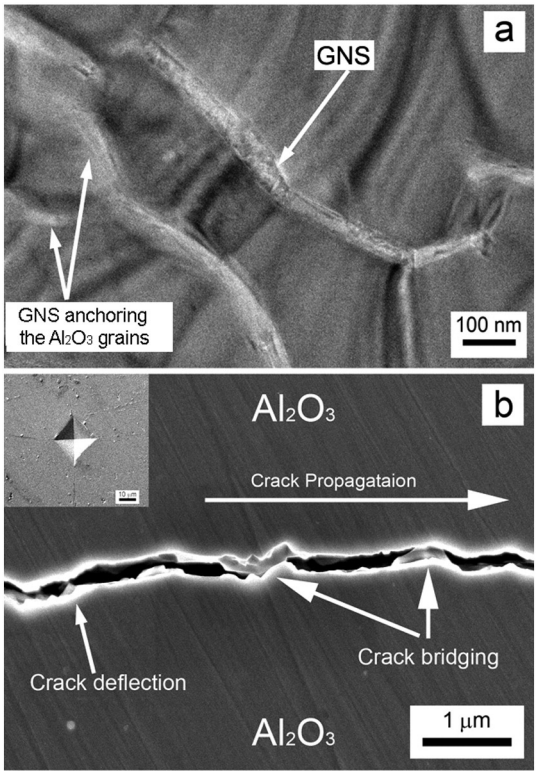

Fig. 7. (a) TEM images representing GNS anchoring interaction with the base matrix grains and (b) SEM image shows GNS bridging the cracked surfaces, Vickers hardness indent in inset.

The firm sticking of GNS to the Al_2O_3 matrix appears to have strengthened the grain boundary area indirectly, causing the fracture to accrue through the Al_2O_3 grains rather than along grain boundaries thus leading to the transgranular failure. Furthermore, the slender edges of the protruded GNS exhibited extremely limited number of graphene layers, whose important role towards greater friction resistance has been theoretically predicted in literature [42]. Presumably, the firm Al_2O_3/GNS interfacial connection held both ends of the GNS prior to the detachment, and then the anchoring mechanism supported the GNS against being pull-out. The combination of these actions allowed the GNS to stretch to a substantial extent during crack opening stage. Depending on its elasticity, an extensibility of 20% strain has been reported for graphene [42,43]. This analysis highlights the direct role of GNS towards arresting the crack progression and stress dissipation through crack-bridging toughening mechanism (Fig. 7b). Therefore, the nanocomposite reinforced with only 0.25 wt.% GNS reached a notable K_{IC} value of 4.1 MPa·m$^{1/2}$, which is 25% higher than that of monolithic Al_2O_3 (K_{IC} = 3.3 MPa·m$^{1/2}$).

The Al_2O_3/0.5GNS nanocomposite sample exhibited relatively larger sized GNS segments (Fig. 5c) after being pulled out from the matrix. A close observation further revealed the discrete multi-layered structure for the GNS with edge thickness of 20–40 nm, as determined from cross-section shown in Fig. 8b. The appearance of these multi-layered GNS structures in the fractured surface (Fig. 8c) thus implies a two-stage toughening mechanism. The toughening imparted by the GNS as it confronted a propagating crack is schematically illustrated in Fig. 8d. As the outermost GNS layers are firmly adhered with the Al_2O_3 matrix grains, it is anticipated that during the initial stage, the flexible GNS will sustain the applied stress (Fig. 8d-i) until the elastic limit is exceeded. At that point, either it is detachment from the matrix or is ruptured at high loads (Fig. 8d-ii), depending on C–C bond strength in GNS and the Al_2O_3/GNS interfacial bond strength whichever is less. In the former case, the load-bearing characteristics of the GNS play an essential role as the applied stress is transferred to inner graphene layers

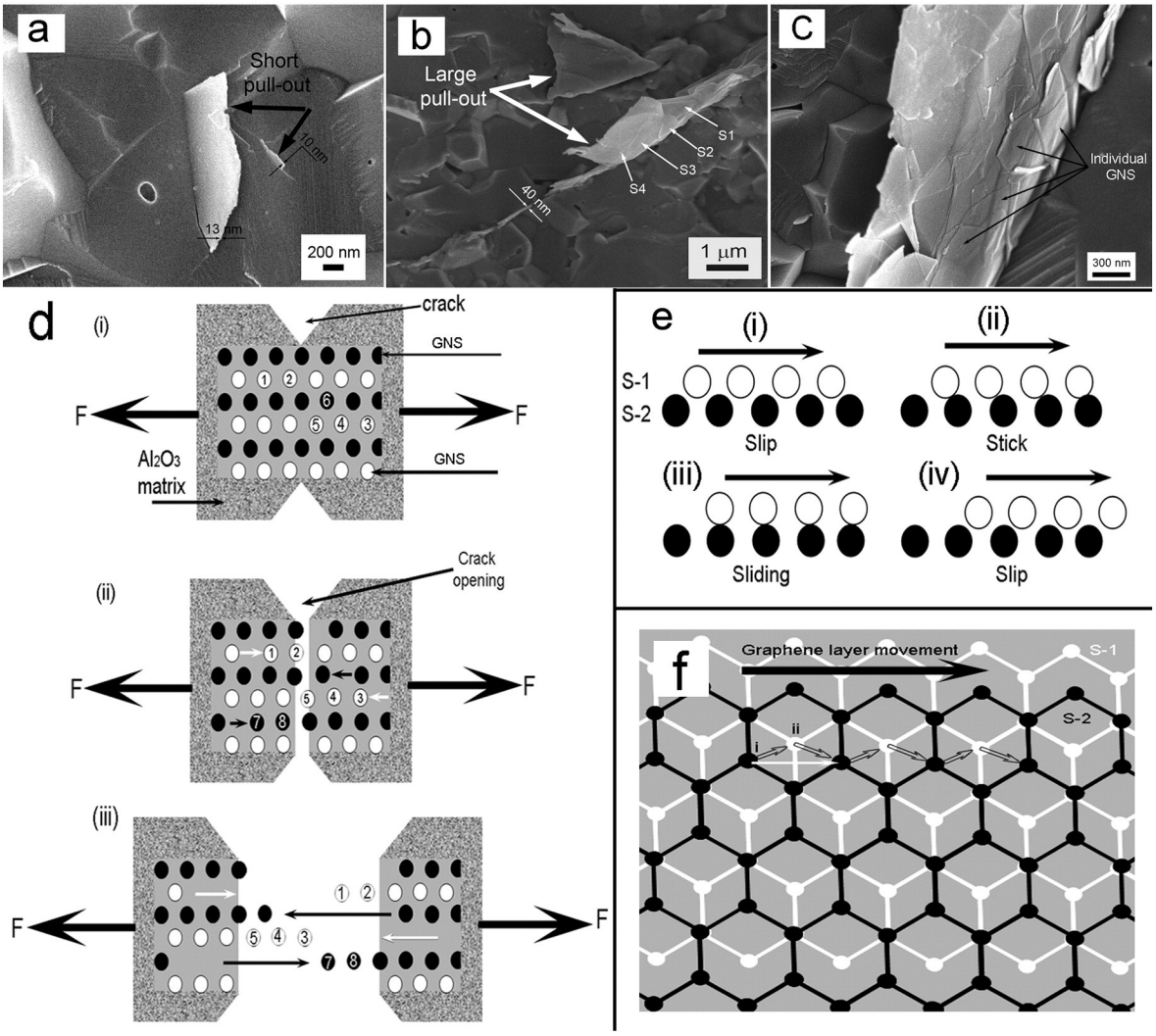

Fig. 8. (a–c) High magnification SEM view of fractured surfaces for different Al_2O_3/GNS nanocomposite specimens: (a) Al_2O_3/0.25GNS showing short GNS pull-out segment and its adhesion with Al_2O_3 matrix, (b) Al_2O_3/0.5GNS with relatively larger sized GNS pull-out areas exhibiting discrete graphene layers (small white arrows), (c) a multi-layered graphene structure. of a pulled out GNS; (d) A schematic model illustrating GNS pull-out toughening mechanism and slip–stick phenomenon in adjacent GNS layers, (e, f) size and top view of the top lattice atoms undergoing slip/stick motion under the influence of applied force.

that are not directly adhered to the ceramic matrix which in turn, can travel long distances via slippage prior to detachment (Fig. 8d-iii) [44–45]. Such delay in layer detachment occurs probably due to slow slithering of layers leading to slip–stick effect (a sudden slip after a period of sticking to a certain position of the surface) and offers complicated inter-layer friction forces as predicted in atomistic simulations [46–48]. Fig. 8e is a schematic representation of a three step slip–stick phenomenon that is likely to have occurred during GNS layers movements in the nanocomposite. Let us denote the top GNS layer (white circles) as S-1 white that slithers over a fixed bottom GNS layer called S-2 (black circles). During the first stage (Fig. 8e-i), the carbon atoms making up the lattice of the S-1 layer slip in the lattice fringe gaps of the underlying S-2 layer with little effort. After slip to a certain distance, however, the S-1 atoms get stuck within the interstitial spacing of the S-2 lattice atoms leading to sticking phenomenon (Fig. 8e-ii) involving chemical bond formation. To overcome sticking forces and to continue further sliding, relatively larger force will be required during the third step (Fig. 8e-iii). The overall atomic movement from such complex nature of stick–slip mechanism will, therefore, be in a zigzag direction (hollow arrows in Fig. 8f), in accordance with the prediction made with the help of atomistic simulation [46]. Such non-identical slip systems, therefore, made it much more energy intensive for the adjacent GNS layers to slide over each other. Moreover, the slip–stick mechanism spreads over a wide area of the GNS surface which leads to formation of extra sliding interfaces during inter-layer movement, hence leading to enhanced lattice atom resistance against sliding and superior friction properties at nanoscale [48,49]. In this way, the larger area of the pulled out GNS seems to inhibit crack propagation, as greater amount of energy will be needed to overcome these friction forces, thus improving the GNS efficiency towards crack-bridging and other toughening mechanisms in the nanocomposite. This is demonstrated by fracture toughness enhancement by means of K_{IC} value from 3.3 (for monolithic Al_2O_3) to 5.7 MPa·$m^{1/2}$, an increase by 72%.

The reason behind the K_{IC} value drop in nanocomposites loaded with higher GNS content (>1.5 wt.%) is most probably the GNS aggregates, as visible in polished (Fig. 4c) and fractured (Fig. 5b) samples and the cross-section of a GNS glut was appeared around 150 nm. Close inspection of a fractograph (Fig. 2d) revealed porous like features at critical locations of GNS–Al_2O_3 junctions depicting almost no adhesion to each other. These microstructural defects obviously would favor the cracks to initiation and to propagate along the grain boundaries, as these aggregates barely contribute in grain boundary strengthening/toughening mechanisms, and resulted in mechanically poor nanocomposites, as represented in Fig. 6. We also compare our K_{IC} results (Fig. 6b) with existing studies in this context and better results in our case are possibly due to using new composite powder mixing methodology and rapid

sintering technology [15,24–26]. Prolonged reaction time was introduced, in this study, which allowed surfactant to thoroughly adsorb on the GNS which led it to disperse well within the Al_2O_3 matrix whereas others merely relied only on either surfactant type or mechanical mixing techniques [22–27]. Furthermore, the fast pressure-assisted HFIHS technology, adopted in this study, works on merging the principles of the SPS (creep and related mechanism) and HP (material diffusion mechanism) processes thereby offered collective advantages of (i) nanocomposite constituents integration down to atomic level for higher densification and (ii) protection of the nanoscale features morphology and structure of the reinforcements in the final nanocomposites to perform proposed toughening mechanism [15,39] thus tough Al_2O_3/GNS nanocomposites could be produced.

3.6. Interface structures

The Al_2O_3/GNS interfacial area at high magnification is presented in Fig. 9 in which both GNS and Al_2O_3 phases can be distinguished by their respective lattice fringe spacing of 0.34 and 0.26 nm that correspond to (002) planes in graphene and (104) planes in Al_2O_3, respectively. The Al_2O_3/GNS interfacial area seems very well bonded (white arrow in Fig. 9a), however, any intermediate second phase could hardly be discriminated. Analysis of the XRD pattern (Fig. 9b) showed characteristic Al_2O_3 crystalline peaks (JCPDS No. 01-078-2426) for sintered monolithic Al_2O_3, whereas a new peak was identified at 26.3° for nanocomposite samples corresponding to crystalline graphite (JCPDS No. 01-075-1621). No other second phase peaks were detected, implying that there has not been any significant chemical reaction between GNS and the Al_2O_3 matrix. We have earlier reported formation of an intermediate thin phase (Al_2OC) at the Al_2O_3/CNT interface for nanocomposites fabricated using hot-pressing [11]. In this context, both CNT and GNS are originated from graphitic structure, and they should behave in a similar manner in terms of chemical activity. Perhaps provision of long hours of reaction spells during hot-pressing or pressure-free sintering allows sufficient time for the Al_2O_3/CNT interface to form an intermediate phase through slow material diffusion mechanism [12,14]; whereas the HFIHS process works on fast sintering leaving the materials very little or almost no time to diffuse [29–31]. Furthermore, the well-bonded GNS with Al_2O_3 is clearly visible in the HR-TEM image in Fig. 9a, and these obvious atomic scale features are similar to those reported for the CNT/Al_2O_3 nanocomposites [11,12,14]. This means that the rapid HFIHS process has most likely contained the possible chemical reactions within only a few atomic layers in our nanocomposites, thus no second phase at the GNS-Al_2O_3 interface was detectable in XRD data. Further advanced microscopic research is warranted to acquire deeper understanding in this intriguing area of nanocomposite technology.

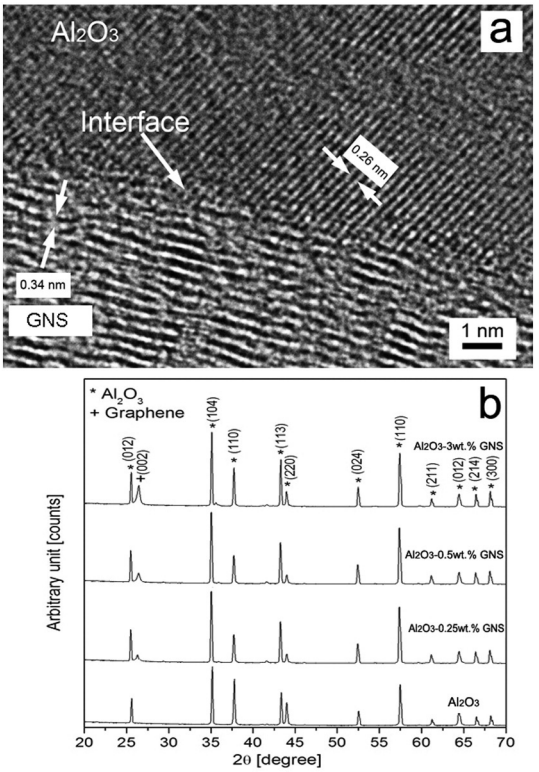

Fig. 9. (a) HR-TEM microstructure of the Al_2O_3/GNS interface showing firm attachment between Al_2O_3 matrix and GNS without any intermediate secondary phase formation and (b) XRD patterns of the monolithic Al_2O_3 and various Al_2O_3/GNS nanocomposites after HFIHS process.

4. Conclusions

Al_2O_3/GNS nanoceramics incorporating 0 to 3.0 weight percent thermally exfoliated graphene nanosheets can be produced through homogenous GNS mixing with Al_2O_3 nanoparticles via an aqueous colloidal chemistry route and subsequently consolidation using a pressure-assisted HFIHS technique. Processing conditions namely 1500 °C sintering temperature, 60 MPa pressure and 3 min holding time, yields samples with near-theoretical densities (>99%). For up to 0.5 wt.% GNS addition, grain size refinement occurred with average size from 1.5 μm (for monolithic Al_2O_3) to 0.8 μm due to grain boundary locking and grain wrapping phenomena by GNS. The effect on microhardness is not much pronounced, rather a drop in microhardness values observed for higher GNS loading levels of 1.5 and 3 wt.%. Reinforcement of the Al_2O_3 matrix with GNS influences its failure behavior by converted from intergranular to the transgranular mode of fracture for up to in the 0.50 wt.% GNS in the nanocomposites with an associated improvement in fracture toughness value by 72%. Owing to their two-dimensional geometry, GNS effectively cover a large area of microstructure through grain anchoring to improve the Al_2O_3/GNS interfacial strength besides promoting crack bridging and crack deflection toughening mechanisms. A theoretical model outlining stick–slip effect arising from GNS elasticity and its complicated inter-layer friction is proposed to account for longer GNS pull-out segments and subsequently superior fracture toughness in such nanocomposites. The firm adhesion between the Al_2O_3 matrix and GNS without formation of any distinct secondary interfacial phase is attributed to the fast HFIHS sintering technique. Al_2O_3/GNS nanocomposites containing relatively higher loading levels of 1.5 and 3 wt.% exhibit deterioration in hardness and fracture toughness due to GNS folding, increased degree of mutual interactions between graphene different nanosheets and more grain boundary porosity.

Acknowledgments

The authors would like to extend their sincere appreciation to the Deanship of Scientific Research at King Saud University for its funding of this research through the Research Group Project no. RGP-VPP-283.

References

[1] C. Rocha, B. Alonso, A. Fernández, C.F. Gutierrez-Gonzalez, R. Torrecillas, A. Zurutuza, Graphene for tough and electro-conductive alumina ceramics, J. Eur. Ceram. Soc. 33 (2013) 3201–3210.
[2] A.G. Evans, Perspective on the development of high-toughness ceramics, J. Am. Ceram. Soc. 73 (1990) 187–206.
[3] J.R. Martinlli, F. Sene, Electrical resistivity of ceramic–metal composite materials: application in crucibles for induction furnaces, Ceram. Int. 26 (2000) 325–335.
[4] L. Osayande, I. Okoli, Fracture toughness enhancement for alumina system: a review, Int. J. App. Ceram. Technol. 5 (2008) 313–323.
[5] J. Llorca, M. Elices, J.A. Celemin, Toughness and microstructural degradation at high temperature in SiC fiber-reinforced ceramics, Acta Mater. 46 (1998) 2441–2453.
[6] F. Yongqing, Y.W. Gu, D. Hejun, SiC whisker toughened Al_2O_3–(Ti,W)C ceramic matrix composites, Scripta Mater. 44 (2001) 111–116.

[7] E. Zapata-Solvas, D. Gómez-García, A. Domínguez-Rodríguez, Towards physical properties tailoring of carbon nanotubes–reinforced ceramic matrix composites, J. Eur. Ceram. Soc. 32 (2012) 3001–3020.
[8] M. Estili, Y. Sakka, Recent advances in understanding the reinforcing ability and mechanism of carbon nanotubes in ceramic matrix composites, Sci. Technol. Adv. Mater. 15 (2014) 064902.
[9] I. Ahmad, B. Yazdani, Y.Q. Zhu, Recent advances on carbon nanotubes and graphene reinforced ceramics nanocomposites, Nanomaterials 5 (2015) 90–114.
[10] J. Cho, A.R. Boccaccini, M.S.P. Shaffer, Ceramic matrix composites containing carbon nanotubes, J. Mater. Sci. 44 (2009) 1934–1951.
[11] S. Sarkar, P.K. Das, Microstructure and physicomechanical properties of pressure-less sintered multi-walled carbon nanotube/alumina nanocomposites, Ceram. Int. 38 (2012) 423–432.
[12] I. Ahmad, A. Kennedy, Y.Q. Zhu, Carbon nanotubes reinforced alumina nanocomposites: mechanical properties and interfacial investigations, Comp. Sci. and Tech. 70 (2010) 1199–1206.
[13] F. Inam, T. Pijis, M.J. Reece, The production of advanced fine-grained alumina by carbon nanotubes addition, J. Eur. Ceram. Soc. 31 (2011) 2853–2859.
[14] I. Ahmad, H. Cao, H. Chen, H. Zhao, A. Kennedy, Y.Q. Zhu, Carbon nanotube toughened aluminium oxide nanocomposites, J. Eur. Ceram. Soc. 30 (2009) 865–873.
[15] H. Porwal, S. Grasso, M.J. Reece, Review of graphene–ceramic matrix composites, Adv. in Appl. Ceram. 112 (2013) 443–454.
[16] K.S. Novoselov, A.K. Geim, S.V. Morozov, D. Jiang, Y. Zhang, S.V. Dubonos, I.V. Grigorieva, A.A. Firsov, Electric field effect in atomically thin carbon films, Science 306 (2004) 666–669.
[17] Bai S, Shen X. Graphene-inorganic nanocomposites. RSC Advances 2012;2:64–98.
[18] H. Shifeng, C. Xin, Effect of carbon black on properties of 0-3 piezoelectric ceramics/cement composites, Curr. Appl. Phys. 9 (2009) 1191–1194.
[19] Y.C. Fan, L.J. Wang, J.L. Li, J.Q. Li, S.K. Sun, F. Chen, L.D. Chen, W. Jiang, Preparation and electrical properties of graphene nanosheet/Al_2O_3 composites, Carbon 48 (21) (2010) 1743–1749.
[20] T. He, J.L. Li, L.J. Wang, J.J. Zhu, W. Jiang, Preparation and consolidation of alumina/graphene composite powders, Mater. Trans. 50 (2009) 749–751.
[21] C.W. Lam, J.T. James, R. McCluskey, S. Arepalli, R.L. Hunter, A review of carbon nanotube toxicity and assessment of potential occupational and environmental health risks, Crit. Rev. Toxicol. 36 (2006) 189–217.
[22] L.S. Walker, E.L. Corral, Toughness in grapheme ceramic composites, ACS Nano 4 (2011) 3182–3190.
[23] J. Dusza, Microstructure and fracture toughness of Si_3N_4 + graphene platelet composites, J. Eur. Ceram. Soc. 32 (2012) 3389–3397.
[24] K. Wang, T. Wei, Preparation of graphene nanosheets/alumina composites by spark plasma sintering, Mater. Res. Bulletin 46 (2011) 315–318.
[25] L. Jain, H.K. Jiang, Mechanical properties of graphene platelets-reinforced alumina ceramics composites, Ceram. Int. 39 (2013) 6215–6221.
[26] H. Porwal, P. Tatarko, S. Grasso, J. Khaliq, I. Dlouhy, M.J. Reece, Graphene reinforced alumina nano-composites, Carbon 64 (2013) 359–369.
[27] B. Yazdani, Y. Xi, I. Ahmad, Y.Q. Zhu, Graphene and carbon nanotube (GNT)-reinforced alumina nanocomposites, J. Eur. Ceram. Soc. 35 (2015) 179–186.
[28] A.R. Khalil, S.W. Kim, Effect of processing parameters on the mechanical and microstructural behavior of ultra-fine Al_2O_3-(ZrO_2 + 8 mol% Y_2O_3) bioceramic densified by high frequency induction heat sintering, Int. J. Appl. Ceram. Technol. 3 (4) (2006) 322–330.
[29] H.C. Kim, D.Y. Oh, I.J. Shon, Sintering of nanophase WC-15 vol% Co hard metals by rapid sintering process, Int. J. Refract. Hard Mater. 22 (2004) 197–203.
[30] S.W. Kim, A.R. Khalil, High-frequency induction heat sintering of mechanically alloyed alumina–yttria-stabilized zirconia nano-bioceramics, J. Am. Ceram. Soc. 89 (4) (2006) 1280–1285.
[31] W. Kim, I.J. Shon, The effect of graphene reinforcement on the mechanical properties of Al_2O_3 ceramics rapidly sintered by high-frequency induction heating, Int. J. Refract. Met. Hard Mater. 48 (2015) 376–381.
[32] W.S. Hummers, R.E. Offeman, Preparation of graphitic oxide, J. Am. Chem. Soc. 80 (1958) 1339-39.
[33] S. Pei, H. Cheng, The reduction of graphene oxide, Carbon 50 (2012) 3210–3228.
[34] I. Ahmad, M. Islam, A.A. Almajid, B. Yazdani, Y.Q. Zhu, Investigation of yttria-doped Al_2O_3 nanocomposites reinforced by multi-walled carbon nanotubes, Ceram. Int. 40 (2014) 9327–9335.
[35] W.C. Oliver, G.M. Pharr, Measurement of hardness and elastic modulus by instrumented indentation: advances in understanding and refinements to methodology, J. Mater. Res. 19 (2) (2004) 3–20.
[36] Y. Fan, M. Estili, G. Igarashi, A. Kawasakia, The effect of homogeneously dispersed few-layer graphene on microstructure and mechanical properties of Al_2O_3 nanocomposites, J. Eur. Ceram. Soc. 34 (2) (2014) 443–451.
[37] G.R. Anstis, P. Chantikul, D.B. Marshal, A critical evaluation of indentation technique for measuring fracture toughness: I, direct crack method, J. Amer. Ceram. Soc. 64 (1981) 533–538.
[38] H.C. Schniepp, J.L. Li, M.J. McAllister, H. Sai, M. Herrera-Alonso, D.H. Adamson, I.A. Aksay, Functionalized single graphene sheets derived from splitting graphite oxide, J. Phys. Chem. B 110 (2006) 8535–8539.
[39] I. Ahmad, M. Islam, F. Xu, S.I. Shah, Y.Q. Zhu, Magnesia tuned multi-walled carbon nanotubes–reinforced alumina nanocomposites, Mater. Character. 99 (2015) 210–219.
[40] J.P. Howe, Properties of graphite, J. Am. Ceram. Soc. 35 (11) (1952) 275–282.
[41] L. Xu, T.B. Ma, Y.Z. Hu, H. Wang, Vanishing stick–slip friction in few-layer graphenes: the thickness effect, Nanotechnology 22 (2011) 285708–285714.
[42] C. Lee, X. Wei, J.W. Kysar, J. Hone, Measurement of the elastic properties and intrinsic strength of monolayer graphene, Science 321 (2008) 385–388.
[43] Guo W, Yin J, Qiu Hu, Xue M. Friction of low-dimensional nanomaterial systems. Friction 2014;2(3):209–25.
[44] A. Richter, R. Ries, R. Smith, M. Henkel, B. Wolf, Diam. Relat. Mater. 9 (2000) 170–184.
[45] Y. Guo, W. Guo, C. Chen, Modifying atomic-scale friction between two graphene sheets: a molecular-force-field study, Phys. Rev. B 76 (2007) 155429.
[46] F. Bonelli, N. Manini, E. Cadelano, L. Colombo, Atomistic simulations of the sliding friction of graphene flakes, Eur. Phys. J. B 70 (2009) 449–459.
[47] Maxim KZ, Jeremy TR, Chad EJ, James CC, Thomas LR, Rory S, Paul ES, Brian HH, Eric S S. Engineering graphene mechanical systems. Nano Lett. 2012;2:4212–18.
[48] M.V. Rastei, B. Heinrich, J.L. Gallani, Puckering stick–slip friction induced by a sliding nanoscale contact, Physical Review Lett. 111 (2013) 084301.
[49] K. Matsushita, H. Matsukawa, N. Sasaki, Atomic scale friction between clean graphite surfaces, Solid State Commun. 136 (2005) 51–55.